Geosci. Model Dev. Discuss., 8, 673–713, 2015
www.geosci-model-dev-discuss.net/8/673/2015/
doi:10.5194/gmdd-8-673-2015

Geoscientific Model Development Discussions
Open Access

S2P3-R (v1.0): a framework for efficient regional modelling of physical and biological structures and processes in shelf seas

R. Marsh[1], A. E. Hickman[1], and J. Sharples[2,3]

[1]University of Southampton, National Oceanography Centre, Southampton, UK
[2]School of Environmental Sciences, University of Liverpool, Liverpool L69 3BX, UK
[3]National Oceanography Centre, Liverpool, Joseph Proudman Building, 6 Brownlow Street, Liverpool L3 5DA, UK

Received: 17 December 2014 – Accepted: 12 January 2015 – Published: 30 January 2015

Correspondence to: R. Marsh (rma@noc.soton.ac.uk)

Published by Copernicus Publications on behalf of the European Geosciences Union.

Abstract

An established 1-dimensional model of Shelf Sea Physics and Primary Production (S2P3) is adapted for regional use in realistic geographical domains over selected years, for selected regions. The S2P3-R framework (v1.0) can be used to efficiently map 3-D physical and biological structures in shelf seas, in particular the tidal mixing fronts that seasonally develop at boundaries between mixed and stratified water. The model has primarily been developed for undergraduate oceanography modules and research projects, providing a practical tool for linking theory and field observations, but it is also useful as an investigative research tool alongside more complex and computationally expensive models. Four different configurations of S2P3-R are described and evaluated, illustrating a range of diagnostics, evaluated where practical with available observations. The model can be forced with daily meteorological variables for any selected year in the reanalysis era (1948 onwards). Example simulations illustrate the considerable extent of synoptic-to-interannual variability in the physics and biology of shelf seas. In discussion, the present limitations of S2P3-R are emphasized, and future model developments are outlined.

1 Introduction

In a global context, the shelf seas are disproportionately productive due to the continuous supply of nutrients (Holt et al., 2009a, and references therein). A variety of models have been developed to explore the processes that shape and maintain productivity. Such models necessarily couple physical and biological processes at high spatial resolution. Operational biogeochemistry and ecosystem models typically represent the system with relatively high complexity and are configured with the finest possible horizontal resolution, e.g., the 7 km Atlantic Margin Model NEMO-ERSEM (AMM7-NE) system (Edwards et al., 2012) – see also http://www.metoffice.gov.uk/research/news/marine-predictions. Such models may perform well alongside observations, but simulations rely on high performance computing resources such that extensive experimental work is consequently not practical.

In contrast to such complex models, the Shelf Sea Physics and Primary Production (S2P3) model (Simpson and Sharples, 2012) exploits the dominance of vertical processes over horizontal processes in shelf seas to efficiently simulate the seasonal cycle of stratification and primary production at a selected location, characterized by a local depth and tidal current amplitude. As summarized at the present hosting website, S2P3 "… simulates the vertical structure of a shelf sea influenced by seasonal heating/cooling, tidal currents and winds. The physics in the model drives a simple primary production (nutrient-phytoplankton, or NP) model, illustrating how phytoplankton growth responds to changes in stratification and mixing" (http://pcwww.liv.ac.uk/~jons/model.htm). In particular, S2P3 is used to simulate the seasonal tidal mixing fronts that develop in mid-latitude shelf seas, at the discontinuity between mixed and seasonally stratified water (Simpson and Hunter, 1974). The computational efficiency afforded by 1-D modelling permits the resolution of physical and biogeochemical structures that are not well represented in operational models with even the finest meshes (e.g., the 7 km mesh of AMM7-NE).

S2P3 was introduced and documented as PHYTO-1D (Sharples, 1999). A more recent version of PHYTO-1D was documented in Sharples (2008). The model is designed for use as an investigative (and educational) tool for exploring the link between the physical structure of the water column and primary biological production in coastal and shelf seas (see zipped material at http://pcwww.liv.ac.uk/~jons/model.htm). S2P3 has been used as a research tool to establish the varying influence of winds and air–sea heat fluxes on inter-annual variability in the timing of stratification and the spring bloom in the northwestern North Sea (Sharples et al., 2006), and to quantify the impact of spring-neap tidal cycles on biological productivity at tidal mixing fronts (Sharples, 2008). In educational contexts, S2P3 and forerunner models have been used for around 10 years in Year 3 undergraduate and masters level postgraduate teaching at the Universities of Southampton and Liverpool, in the UK.

GMDD
8, 673–713, 2015

Introduced here, S2P3-R is a framework for using S2P3 v7.0 to efficiently model 3-D physical and biological structure in shelf seas, for selected years during the reanalysis era (Kalnay et al., 1996). The development of S2P3-R has facilitated an expansion of S2P3 modelling to a range of realistic settings and time periods, thus facilitating simulation of 3-D structure in real time, for quick investigation of ongoing changes and detailed fieldwork planning. Educational possibilities are also extended for both group and individual project work, involving two taught modules (ongoing) and five individual research projects to date.

In the remainder of the paper, we first outline the S2P3-R framework. We start with a brief description of the physical and biological components of S2P3, followed by details of the modified source code, model performance and diagnostic options. This is in turn followed by details on model setup in different domains (horizontal meshes and tidal forcing), and the specification of meteorological forcing. We then evaluate model simulations for four different regions, undertaken and diagnosed using the new framework. In discussion, some important caveats are emphasized, and we outline the prospects for development of S2P3 itself, within S2P3-R, to implicitly include lateral processes that become influential near coasts and the shelf break and to resolve variability in turbidity and phytoplankton physiology.

2 The S2P3-R framework

2.1 S2P3

Here, we provide a brief description of the physical and biological components of S2P3, emphasizing key equations. Forward time stepping is explicit throughout, with time-steps, Δt, constrained by the diffusive stability criterion, $\Delta t < \Delta z^2/2N_z$, given depth intervals, Δz, and vertical eddy viscosity, N_z. The model is very little changed from the original description provided by Sharples (1999), and for a more detailed model description, the reader is referred to that paper.

2.1.1 Physical model

Central to the physics of S2P3 is a turbulence closure scheme, for which the prognostic variable is turbulent kinetic energy (TKE), formally defined as $q^2/2$, where q is the turbulent intensity, or velocity scale ($\mathrm{m\,s^{-1}}$). For a tidal current with x and y components u and v, the tendency of TKE is expressed as:

$$\frac{\partial}{\partial t}\left(\frac{q^2}{2}\right) = \frac{\partial}{\partial z}\left(K_q \frac{\partial}{\partial z}\left(\frac{q^2}{2}\right)\right) + N_z\left[\left(\frac{\partial u}{\partial z}\right)^2 + \left(\frac{\partial v}{\partial z}\right)^2\right] + K_z\left(\frac{g}{\rho}\frac{\partial \rho}{\partial z}\right) - \frac{q^3}{B_1 l} \tag{1}$$

where ρ is density, quadratic in temperature T ($\rho = 1028.11 - 6.24956 \times 10^{-2} T - 5.29468 \times 10^{-3} T^2$, assuming a constant salinity of 35.00), B_1 is a constant of the closure scheme, K_q is the vertical eddy diffusivity for TKE, K_z is the vertical eddy diffusivity for other scalar properties, and l is an eddy length-scale ($l = \kappa z(1 - z/h)^{0.5}$, at depth z, given total depth h and von Karmen's constant $\kappa = 0.41$). Tides and winds force the TKE profile for given boundary conditions:

$$q^2_{z=h} = B_1^{2/3} \frac{\tau_\mathrm{s}}{\rho_{z=h}}; \tag{2a}$$

$$q^2_{z=0} = B_1^{2/3} \frac{\tau_\mathrm{b}}{\rho_{z=0}} \tag{2b}$$

where τ_s is the surface ($z = h$) stress due to the wind, and τ_b is the near-bottom ($z = 0$) stress due to tidal currents. The x and y components of wind stress are obtained as:

$$\tau_\mathrm{sx} = -c_\mathrm{d} \rho_\mathrm{a} u_\mathrm{w} \sqrt{\left(u_\mathrm{w}^2 + v_\mathrm{w}^2\right)}; \tag{3a}$$

$$\tau_\mathrm{sy} = -c_\mathrm{d} \rho_\mathrm{a} v_\mathrm{w} \sqrt{\left(u_\mathrm{w}^2 + v_\mathrm{w}^2\right)} \tag{3b}$$

GMDD
8, 673–713, 2015

given a drag coefficient c_d ($c_d = (0.75 + 0.067\,w) \times 10^{-3}$, for wind speed w), air density ρ_a ($= 1.3\,\mathrm{kg\,m^{-3}}$), and u_w and v_w, the x and y components of wind. The x and y components of near-bottom stress are obtained as:

$$\tau_{bx} = -k_b \rho_0 u_1 \sqrt{\left(u_1^2 + v_1^2\right)}; \tag{4a}$$

$$\tau_{by} = -k_b \rho_0 v_1 \sqrt{\left(u_1^2 + v_1^2\right)} \tag{4b}$$

given a drag coefficient k_b ($= 0.003$), representative density for seawater ρ_0 ($= 1025\,\mathrm{kg\,m^{-3}}$), and u_1 and v_1, the x and y components of the current 1 m above the seabed. See Sharples (1999) for further details on the subsequent calculation of N_z, K_z and K_q.

In addition to mixing, the water column is locally heated and cooled. The tendency of temperature, T, is obtained at each depth level as:

$$\frac{\partial T}{\partial t} = \frac{\partial}{\partial z}\left(K_z \frac{\partial T}{\partial z}\right) + Q_h(z) \tag{5}$$

where z is height above the seabed, T is temperature, and $Q_h(z)$ is the net heating at depth z.

Heat fluxes are formulated as follows. We first define a surface net heat flux (Q_{net}) as the sum of incoming shortwave radiation (Q_{SW}), long-wave back radiation (Q_{LW}), and latent and sensible heat exchange with the atmosphere (Q_{sens} and Q_{lat}):

$$Q_{net} = Q_{SW} - (Q_{LW} + Q_{sens} + Q_{lat}) \tag{6}$$

Incoming shortwave radiation, irradiance in the presence of clouds, is calculated as:

$$Q_{SW} = (1.0 - 0.004C - 0.000038C^2)Q_{SW,c\text{-}s} \tag{7}$$

where C is cloud fraction, and clear sky irradiance, $Q_{\mathrm{SW,c\text{-}s}}$, is obtained as:

$$Q_{\mathrm{SW,c\text{-}s}} = S(1-\alpha)f(\theta,t)(1-\kappa_{\mathrm{SW}}) \tag{8}$$

where S is the solar constant ($= 1368\,\mathrm{W\,m^{-2}}$), α is an atmospheric albedo ($= 0.24$), $f(\theta,t)$ is a function representing the daily and seasonal variation in day length at latitude θ, and κ_{SW} is a short-wave absorption coefficient ($= 0.06$). Long-wave radiation is calculated as:

$$Q_{\mathrm{LW}} = \varepsilon_{\mathrm{LW}}(1.0 - 0.6\times10^{-4}C^2)(0.39 - 0.05q^{0.5})\sigma T^4 \tag{9}$$

where $\varepsilon_{\mathrm{LW}}$ is long-wave emissivity ($= 0.985$), q is vapour pressure ($q = Rq_{\mathrm{s}}$, given saturated vapour pressure $q_{\mathrm{s}}(T)$ and relative humidity R), and σ is the Stefan–Boltzmann constant ($\sigma = 5.67\times10^{-8}\,\mathrm{W\,m^{-2}\,K^{-4}}$). Sensible heat flux is calculated using the bulk formula:

$$Q_{\mathrm{sens}} = \rho_{\mathrm{a}} c_p C_h U(T_{\mathrm{s}} - T_{\mathrm{a}}) \tag{10}$$

where c_p is the specific heat capacity of air ($c_p = 1004\,\mathrm{J\,kg^{-1}\,K^{-1}}$), C_h is a transfer coefficient ($C_h = 1.45\times10^{-3}$), U is surface wind speed, T_{s} is the sea surface temperature, and T_{a} is surface air temperature. Latent heat flux is calculated using the bulk formula:

$$Q_{\mathrm{lat}} = \rho_{\mathrm{a}} L_v C_e U(q_{\mathrm{s}} - q) \tag{11}$$

where L_v is the specific heat capacity of air ($L_v = 2.5\times10^6 - 2.3\times10^3 T_{\mathrm{s}}$), and C_e is a transfer coefficient ($C_e = 1.5\times10^{-3}$).

The surface net heat flux is partitioned down the water column as follows. The red end of the spectrum, 55 % of shortwave radiation, is assumed to be absorbed at the top depth level, hence the surface heating, $Q_{\mathrm{h,0}} = 0.55Q_{\mathrm{SW}} - (Q_{\mathrm{LW}} + Q_{\mathrm{sens}} + Q_{\mathrm{lat}})$. The

GMDD
8, 673–713, 2015
Efficient modelling of shelf seas
R. Marsh et al.

remaining 45 % of insolation is available for heating at lower levels, distributed exponentially throughout the water column as a heating rate $Q_\mathrm{h}(z)$, according to:

$$\frac{\partial Q_\mathrm{h}}{\partial z} = -Q_\mathrm{h}(z)(\lambda_0 + \varepsilon X_T(z)) \tag{12}$$

where λ_0 is an attenuation coefficient ($\lambda_0 = 0.1\,\mathrm{m}^{-1}$) and ε is a pigment aborption cross-section ($\varepsilon = 0.012\,\mathrm{m}^2\,(\mathrm{mg\,chl})^{-1}$), accounting for shading due to $X_T(z)$, the local chlorophyll *a* (chl *a*) concentration ($\mathrm{mg\,chl\,m}^{-3}$), taking $X_T(z) = q^{\mathrm{chl}} P_\mathrm{C}$, for cell chl *a* : carbon ratio, q^{chl} ($0.03\,\mathrm{mg\,chl\,(mg\,C)}^{-1}$), and carbon concentration, P_C (see below).

2.1.2 Biological model

Phytoplankton is modelled in terms of an equivalent carbon concentration (P_C, units $\mathrm{mg\,C\,m}^{-3}$) and internal cellular nitrogen (P_N). In each grid cell, P_C tendency is due to the net effect of vertical mixing, growth and grazing, according to:

$$\frac{\partial P_\mathrm{C}}{\partial t} = \frac{\partial}{\partial z}\left(K_z \frac{\partial P_\mathrm{C}}{\partial z}\right) + \mu P_\mathrm{C} - G P_\mathrm{C} \tag{13}$$

given a grazing impact rate G, and a growth rate, μ, that is a function of photosynthetically-active radiation:

$$\mu = \mu_\mathrm{m}\left(1 - e^{-(\alpha I_\mathrm{PAR}\theta/\mu_\mathrm{m})}\right) - r^B \tag{14}$$

where α is the maximum quantum yield, I_PAR is the light availability, θ is the chl *a* : carbon ratio, r^B is the respiration rate, and the maximum growth rate, μ_m, is given by:

$$\mu_\mathrm{m} = 1.16 \times 10^{-5}\left(\frac{Q - Q_\mathrm{sub}}{Q_\mathrm{m} - Q_\mathrm{sub}}\right) 0.59\mathrm{e}^{0.0633T} \tag{15}$$

where $Q = P_\mathrm{N}/P_\mathrm{C}$ is the cell nitrogen quota, Q_sub is the subsistence nutrient : carbon quota, and Q_m is the maximum cell quota. The tendency for phytoplankton nitrogen (P_N) is similarly described as:

$$\frac{\partial P_\mathrm{N}}{\partial t} = \frac{\partial}{\partial z}\left(K_z \frac{\partial P_\mathrm{N}}{\partial z}\right) + uP_\mathrm{C} - GP_\mathrm{N} \tag{16}$$

where the uptake rate u is obtained as a Michaelis–Menton function of the dissolved inorganic nitrogen concentration (DIN):

$$u = \left[u_\mathrm{m}\left(1 - \frac{Q}{Q_\mathrm{m}}\right)\frac{\mathrm{DIN}}{(k_\mathrm{u} + \mathrm{DIN})}\right] + \begin{cases} \mu Q, & \mu < 0 \\ 0, & \mu \geq 0 \end{cases} \tag{17}$$

given k_u, a half saturation coefficient for nutrient uptake, and u_m, a maximum nutrient uptake rate. The uptake of nitrogen leads to a tendency in dissolved inorganic nitrogen (DIN):

$$\frac{\partial \mathrm{DIN}}{\partial t} = \frac{\partial}{\partial z}\left(K_z \frac{\partial \mathrm{DIN}}{\partial z}\right) - \mu P_\mathrm{C} + eGP_\mathrm{N} \tag{18}$$

where e is the fraction of grazed phytoplankton cellular nitrogen recycled immediately back into the dissolved nitrogen pool.

Water column nitrogen is constantly restored towards an initial winter concentration, DIN_0 ($\mathrm{mmol\,m^{-3}}$), by a flux of inorganic nitrogen from the seabed:

$$\frac{\partial \mathrm{DIN}_1}{\partial t} = \frac{f_\mathrm{DIN}}{\Delta z}\left(1 - \frac{\mathrm{DIN}_1}{\mathrm{DIN}_0}\right) \tag{19}$$

where DIN_1 is the dissolved nitrogen in the bottom depth cell of the model grid, Δz (m) is the thickness of the model grid cell, and f_DIN ($\mathrm{mmol\,m^{-2}\,s^{-1}}$) is the maximum flux of dissolved nitrogen from the seabed into the bottom depth cell.

The values of biological parameters (G, μ_m, θ, r^B, Q_sub, α, u_m, Q_m, k_u, e, DIN_0, f_DIN) are as listed in Table I of Sharples (2008).

GMDD
8, 673–713, 2015

2.2 Modified S2P3 source code, performance and diagnostics

For the S2P3-R framework, we modified the Fortran 90 source code of S2P3 v7.0, which includes additional commands and subroutines to facilitate the Winteracter Fortran GUI toolset (Interactive Software Services Ltd., www.winteracter.com), the model being supplied with a text book (Simpson and Sharples, 2012) as an executable application that runs under the Windows operating system. This source code was modified for compilation and execution in a Unix environment by removing GUI-related lines of code. These changes are solely to facilitate compilation and execution in Unix environments, and S2P3 is thus far unchanged as a scientific tool.

Within the new framework, S2P3 can be used to generate geographically specific maps, sections and time series, with varying run-time implications on a single processor. Maps typically comprise 5000–20 000 grid-points, while sections comprise 10–100 grid-points. For a given year (see below), maps can take over a day to generate (depending on the extent of shallower water, where shorter time-steps are necessary), while sections typically take a few minutes, and annual time series at a single location typically take a few seconds. It would be natural and straightforward to deploy S2P3 in "map" and "section" mode across multiple processors (using e.g., HTCondor – see http://research.cs.wisc.edu/htcondor/), but this has not been done here.

Default mapped variables are presently limited to mid-summer surface–bottom temperature difference, annual-mean surface heat flux, and annual net production, although other quantities, such as the mid-summer sub-surface chl *a* maximum, or SCM, have been mapped. The option for simulating sections is motivated by opportunities for direct comparison with measurements obtained through surveys and cruises. In selecting to simulate section data, constant depth intervals are specified for plotting on a regular distance-depth mesh without the need for interpolation. The option for time series at single locations is motivated by the availability of time series at repeat CTD stations and moorings. Finally, we save daily horizontal distributions of physical and

GMDD
8, 673–713, 2015

biological variables for selected periods, to generate animations that yield a range of insights not so easily appreciated with individual maps or sections.

FORTRAN programmes are used to post-process model data for plotting, and MATLAB scripts are used to plot model variables (as used to prepare the figures and animations presented here). Example MATLAB plotting scripts are provided together with the source code and other ancillary programmes and data files in s2p3-reg.zip (see Sect. 5).

2.3 Regional configurations

Four domains have so far been developed and tested, for reasons that are outlined in turn. Figure 1 shows the bathymetry, while Table 1 specifies the boundaries, resolution, tidal forcing and initial temperature, for each domain. In an initial stage of development, S2P3-R was developed for the northwest European shelf domain. Development of the three other domains has been motivated by ongoing research projects (climate and ecosystem change in the northern North Sea; tidal mixing fronts in the shelf seas around China) and ongoing fieldwork (annual surveys of the tidal mixing front south of Cornwall).

Bathymetry is typically in the range 50–100 m across most of the northwest European shelf (Fig. 1a). However, some important details are emphasised for the other three domains: general deepening towards the north (depths varying in the approximate range 50–150 m) in the North Sea (Fig. 1b); a shallower inshore zone (depths < 30 m) in the Western English Channel (Fig. 1c); a secondary shelf break (descending 50–100 m) in the East China Sea (Fig. 1d). At very high resolution, some artefacts of bathymetric surveying are apparent as linear features in the bathymetry south of Cornwall (Fig. 1c).

For the northwest European shelf (including the sub-region around Scotland), bathymetry and current amplitudes for the leading three tidal constituents (M2, S2, N2 – see Fig. S1 in the Supplement) were obtained from the POLCOMS model (e.g., Holt et al., 2009b). For the Western English Channel, bathymetry is extracted from the

ETOPO1 global relief model (Amante and Eakins, 2009) and tidal current amplitudes are interpolated from the POLCOMS dataset. For the East China and Yellow Seas, current amplitudes for the leading 13 tidal constituents were generated using OTPS (OSU Tidal Prediction Software), based on the inverse method developed by Egbert et al. (1994) and Egbert and Erofeeva (2002), and bathymetry is selected within the OTPS system. Opting to use the leading five constituents for this region, S2P3 was adapted to include the two diurnal constituents, O1 and K1, in addition to the semi-diurnal constituents S2, M2 and N2 (see Fig. S2).

One further distinction in regional setup concerns initial temperatures. At 1 January of each year, the water column is presumed mixed everywhere. In the default model, initial temperature is 10.1 °C at all depths, appropriate for the Celtic Sea. This initial temperature is also appropriate for the Western English Channel, but to limit annual-net heat fluxes within $\pm 10\,\mathrm{W\,m^{-2}}$ at most grid-points (see below), initial temperature is decreased to 7.1 °C for the shelf seas around Scotland. Sensitivity tests illustrate the importance of choosing a reasonable value for initial temperature – see Fig. S3. If the initial temperature around Scotland is too high (Fig. S3a), the net heat fluxes fall below $-10\,\mathrm{W\,m^{-2}}$ across much of the domain, especially to the north, while if the temperature is too low (Fig. S3b), heat fluxes exceed $10\,\mathrm{W\,m^{-2}}$ at most locations. Only if the initial temperature is accurate to within around 1 °C do we avoid strong annual net cooling or heating (Fig. S3c). For the China Seas, we increased the initial temperature to 15.1 °C and then ran two consecutive years, analysing the second year, in order to establish realistic initial conditions across the wider domain (on 1 January of the second year), respecting a degree of wintertime stratification in this region.

2.4 Meteorological forcing

In addition to tidal mixing, S2P3 is forced with surface heat fluxes and wind stirring. Heat is gained by shortwave radiation and lost via long-wave back-radiation, sensible and latent heat fluxes – see Eq. (6). Shortwave radiation varies with latitude and time of year, and decreases with fractional cloud cover – see Eqs. (7) and (8). Long-wave radiation varies with sea surface temperature and cloud cover – see Eq. (9). Sensible and latent heat losses vary with air temperature, wind speed and relative humidity according to bulk formulae – see Eqs. (10) and (11).

Daily values for the four necessary meteorological variables are provided in a single ASCII file. Sharples (2008) uses climatological meteorological data for the Celtic Sea, while Sharples et al. (2006) use meteorological data for 1974–2003 from weather stations in the vicinity of a study site in the northwestern North Sea. Here, we use NCEP Reanalysis data provided by the NOAA/OAR/ESRL PSD, Boulder, Colorado, USA, from their website at http://www.esrl.noaa.gov/psd/. These data are routinely updated to within a day or so of the present time, and span the period from 1948. The data is provided on a 2.5° global mesh, so each domain is forced everywhere with meteorological data from a single 2.5° grid square, central to that region. Coordinates of selected grid squares are listed in Table 1.

Figure 2 illustrates time series of meteorological variables for the four domains. In initial testing, for the northwest European shelf, we use the "default" Celtic Sea climatology (Sharples, 2008). For the other three domains, data for 2013 are shown for example. Note the extent of high-frequency synoptic variability in these cases, in particular for relative humidity, cloud fraction and wind speed. Also note that the UK spring of 2013 was exceptionally cold, hence air temperatures (for the two sub-domains of the UK shelf) considerably below the Celtic Sea climatological average. Also note considerable contrast between the maritime and continental climates, for the European shelf and China Seas respectively.

3 Model evaluation in the new framework

3.1 Northwest European shelf

Figure 3 shows a summary of fields obtained for a simulation using the northwest European shelf domain. Figure 3a shows the annual-mean Hunter–Simpson param-

GMDD
8, 673–713, 2015

eter, $\log_{10}(h\,u^{-3})$, where h is the local depth and u is the amplitude of the local tidal current. Previous studies (starting with Simpson and Hunter, 1974) have established a threshold value of around 2.7, below (above) which the water column is well mixed (stratified). $\mathrm{Log}_{10}(h\,u^{-3})$ is generally below 2.7 throughout the southern North Sea, and across much of the eastern English Channel and the Irish Sea. These regions are indeed well mixed throughout summer, as evident in near-zero surface–bottom temperature differences for mid-July, shown in Fig. 3b. Elsewhere, stratification is established, and the model hence simulates a set of fronts between mixed and stratified water that are clearly observed in satellite data (see Fig. 8.1 in Simpson and Sharples, 2012 – also indicated in Fig. 3a): the Islay front between Northern Ireland and Scotland (A); the Western Irish Sea front enclosing a seasonally-stratified region of the Irish Sea (B); part of the Cardigan Bay front (C); the St George's Channel front between Wales and Ireland (D); the Ushant and Western English Channel front between southwest England and Brittany, France (E). The model also simulates a front observed between the seasonally-stratified northern North Sea and the permanently mixed southern North Sea, including the Flamborough frontal system (Hill et al., 1993, and references therein), also indicated (F) in Fig. 3a.

A limitation of the simulation presented in Fig. 3 is the use of default climatological meteorological forcing, originally set up for simulating tidal mixing fronts in the Celtic Sea. This has important consequences for local heat balances, evaluated here with the annual-mean surface net heat flux, shown in Fig. 3c. In the central Celtic Sea (south of Ireland), the net heat flux is slightly positive, in the range 0–5 $\mathrm{W\,m^{-2}}$. Elsewhere, one might expect that a warmer (cooler) sea surface will lead to stronger net heat loss (gain), via sensible and latent heat fluxes. However, the imbalance reaches a maximum of 10 $\mathrm{W\,m^{-2}}$ in the warm southwest English Channel (net heating) and a minimum of $-10\,\mathrm{W\,m^{-2}}$ in the cool northern North Sea (net cooling). This is consistent with insolation levels at these latitudes that are respectively higher and lower than that for the Celtic Sea. Such imbalances are also a consequence of specifying the same initial temperature everywhere (see Sect. 2.2), such that the northern North Sea is initially too warm (so must lose heat over the seasonal cycle), and the southwest English Channel is initially too cool (so must gain heat). Net heat fluxes are also notably positive in some regions that are well mixed all year round, in particular the Irish Sea and parts of the English Channel, consistent with enhanced heat storage due to mixing throughout the water column of heat gained in summer (Simpson and Bowers, 1984).

We have also experimented, on the northwest European shelf domain, with spatially discriminate initial temperature and meteorological forcing, the latter respecting variation of NCEP reanalysis data (per 2.5° grid square) across the domain. While this approach has the potential to restrict net heat fluxes closer to zero at all locations, it can also introduce artifacts to the forcing depending on how the NCEP data is interpolated to the relatively fine 12 km mesh of S2P3-3-D (not shown here).

Depending on temperature and the co-availability of photosynthetically active radiation (PAR) and nutrients, the model simulates primary production. Annual net carbon production per unit area is shown in Fig. 3d and simulated surface chl *a* is compared to satellite observations in Figs. S4 and S5. The model reproduces key aspects of the temporal and spatial variability in primary production and chl *a* across the shelf. Where aspects are not reproduced, we suggest (in Sect. 4) areas for future model development.

Surface production rates (Fig. 3d) and chl *a* concentrations (Fig. S4) are especially high in shallow coastal water that remains well mixed for most/all of the year, where nutrient is consequently continuously re-supplied from the seabed, and PAR levels are sufficient at all depths to maintain photosynthesis. We have limited confidence in the simulated primary production and chl *a* close to the coasts, for two specific reasons. We presently do not account for the strong influence near many coasts of freshwater (runoff), which has an important stratifying influence on the water column. We also neglect the higher turbidity caused by non-algal particles that can reduce PAR below a level necessary to sustain photosynthesis, e.g., where sediment loads are relatively high in shallow regions of vigorous mixing, such as the southern North

GMDD
8, 673–713, 2015
Efficient modelling of shelf seas
R. Marsh et al.

Sea. Recognizing this model limitation, we choose not to plot model output in water shallower than 30 m in Figs. 3 and S4.

Moving towards stratified regions, annual-mean carbon production rates generally decline, although remain above 55 $\mathrm{g\,C\,m^{-2}\,year^{-1}}$ at most locations due to the combined result of the major spring and minor autumn blooms (see below), complemented by elevated productivity throughout summer at the thermocline, associated with the development and persistence of the sub-surface chl *a* maximum (SCM). Primary production rates during the spring bloom (not shown) reach 40 $\mathrm{g\,C\,m^{-2}\,mon^{-1}}$ or 1333 $\mathrm{mg\,C\,m^{-2}\,d^{-1}}$, in line with observed magnitudes in the order of 1000 $\mathrm{mg\,C\,m^{-3}\,d^{-1}}$ (Rees et al., 1999). Summertime chl *a* and primary production are low in the surface mixed layer, consistent with observed values of <1 mg chl *a* $\mathrm{m^{-3}}$ and 5–30 $\mathrm{mg\,C\,m^{-3}\,d^{-1}}$, respectively (Joint et al., 2000; Hickman et al., 2009). Simulated surface chl *a* concentrations are broadly consistent with satellite observations, although values are typically double those observed (see Figs. S4 and S5). The model does not reproduce the enhanced primary production and chl *a* observed in the surface at the Celtic Sea shelf break (e.g., compare Figs. S4 and S5, for April and May), because it does not include specific physical processes, such as the internal tide, that are important for vertical nutrient supply to the surface in these regions (Sharples et al., 2007).

Following the spring bloom, surface productivity and surface chl *a* concentrations remain elevated (above background values) near three tidal mixing fronts in particular – the Ushant and Western English Channel front, the Islay front, and the St George's Channel front – for June–September in the simulation (Fig. S4) and for May–July in the observations (Fig. S5). Surface chl *a* concentrations decline towards more stratified waters, coincident with deepening of the SCM away from fronts and associated zones of spring-neap frontal adjustment (Pingree et al., 1978; Weston et al., 2005; Hickman et al., 2012). At the Ushant Front, predicted peak July primary production of 80–100 $\mathrm{mg\,C\,m^{-3}\,d^{-1}}$ is considerably smaller than in situ measurements of 59–126 $\mathrm{mg\,C\,m^{-3}\,h^{-1}}$ (implying daily production of around 1000 $\mathrm{mg\,m^{-3}\,d^{-1}}$), for surface waters at a frontal station in late July (Holligan et al., 1984). However, the model es-

GMDD
8, 673–713, 2015

Efficient modelling of shelf seas

R. Marsh et al.

timates are intermediate between corresponding surface observations for mixed and stratified waters (reported in Holligan et al., 1984), emphasizing the very localized character of frontal productivity, which is not easily captured with our relatively coarse model resolution (here around 12 km) and in the absence of horizontal processes that may lead to convergence of material at the front.

In the southern Irish Sea and south of the Islay front, simulated surface chl *a* concentrations are notably very low, at around 0.1 mg chl *a* m^{-3} (see Fig. S4). These low values are found in regions where the tidal current amplitude is especially strong (see Fig. S1) in water that is sufficiently deep (~ 100 m, see Fig. 1a) for PAR to fall below a threshold value within the well-mixed water column (Fig. 3b). So in spite of very high nutrient levels throughout the year (not shown), light is a severe limit on photosynthesis and hence productivity. This aspect of the simulation is inconsistent with surface chl-a concentrations of around 1 mg chl *a* m^{-3} observed in this region (Fig. S5; Pemberton et al., 2004; Moore et al., 2006). A likely explanation is that the model does not resolve photo-acclimation, the known ability of phytoplankton to acclimate to ambient light conditions (e.g. Geider et al., 1997), and so does not resolve the photo-physiological differences between stratified and mixed water columns (Moore et al., 2006). Dissolved inorganic nitrate (DIN) concentrations in the northwest European shelf region during winter and in the bottom mixed layer during summer (not shown) are 5–6 mmol m^{-3}, consistent with observed values around 6–9 mmol m^{-3} (Joint et al., 2001; Hickman et al., 2012).

To illustrate typical vertical structure across a mid-summer tidal mixing front, Fig. 4 shows observations and corresponding simulations for day 215 (3 August) of 2003, along a section through the Celtic Sea front (Fig. 4a), located at around 52° N. The temperature structure (Fig. 4b and c) illustrates stratified water south of 52° N, with mixed water to the north. DIN concentrations are high in mixed water and in the lower layer of the stratified water, and depleted in the surface layer of the stratified water (Fig. 4d and e). Chl *a* concentrations reach a surface maximum at the front, with elevated values extending southwards in the model – the SCM supported by a weak diffusive DIN flux across the thermocline (Fig. 4f and g). In broad terms, the model reproduces the observations, although the mixed water is about 1 °C cooler than observed, and DIN and chl *a* concentrations are about 50 % higher at most depths.

3.2 Around Scotland

We now use NCEP daily meteorological forcing centred on 0° E, 57.5° N to simulate seasonal cycles of stratification across the domain around Scotland. The example of summer stratification, annually for 2004–2013, is shown in Fig. S6. The distribution of mixed and stratified waters evident in each year bear strong resemblance to that in Fig. 3b, although results are more accurate with local meteorological forcing and lower initial temperature. Interannual variability in stratification is evident, weakest in 2008 and strongest on 2013, with surface–bottom temperature differences varying by around 2 °C between these two extreme years. Although the same daily meteorological variables are specified at all grid-points, interannual differences are not spatially uniform, as stratification develops uniquely at each grid-point, and there is also scope for some feedback in anomalous turbulent fluxes via the development of anomalous sea surface temperatures.

For comparison with published data, we simulate surface and bottom temperatures observed with moorings at 1.25° W, 56.25° N (2001) and 1.5° W, 56.25° N (2002), as previously modeled by Sharples et al. (2006). The seasonal cycles in Fig. 5, characterized by stratification during days 110–255 (2001) and days 100–275 (2002), bear close resemblance to the observations and previous model simulations (see Figs. 2 and 3 in Sharples et al., 2006).

3.3 Western English Channel

For 1 May to 7 October of 2013, selected daily model fields are saved and animated (see Supplement Part B, “Example Animation”, and accompanying commentary text). A wide range of phenomena are evident in the animation, including the earliest establishment of stratification during May, expressed as a surface–bottom temperature difference, and the rapid uptake of surface DIN, which declines to near-zero concentrations with the development of a spring bloom (high surface chl *a* levels) that peaks in early-mid June. We note that the exceptionally cold spring of 2013 substantially delayed the onset of stratification and the spring bloom (also suggested by satellite data – not shown). The spring-neap cycle of stronger mixing (on spring tides) and strengthened stratification (on neap tides) causes ~ 14 day "beating" of chl *a* concentration, between low values on spring tides and high values on neap tides, most notably at the front between inshore mixed and offshore stratified waters off southwest Cornwall throughout June and July.

To illustrate the interannual variability of summer stratification, Fig. 6 shows surface–bottom temperature differences on day 190 (8 or 9 July) of 2002–2013. The region is characterized by mixed water to the northwest associated with locally strong tidal current amplitudes (see Fig. S1), and stratified water to the southwest (where tides are weaker), with a secondary area of stratification centred around 4.5° W 50.1° N (coincident with a local minimum in tidal current amplitude). The water column remains mixed all year round in shallow water close to the coast, at most locations and in most years. A complex arrangement of mixed and stratified water is simulated in the northeast of the region, associated with highly variable bathymetry (see Fig. 1c). When a cold spring is followed by a warm summer (e.g., 2006, 2010, 2013), stratification is particularly strong, with surface–bottom temperature differences reaching almost 7 °C in the southwest of the region.

To locally validate the simulation, we use observations at L4 (50°15.00′ N, 4°13.02′ W) and E1 (50°02.00′ N, 4°22.00′ W), hydrographic stations that have been occupied weekly and monthly, respectively, as part of the Western Channel Observatory (http://www.westernchannelobservatory.org.uk/data.php), where seasonal cycles of stratification and phytoplankton dynamics have been extensively studied (Smyth et al., 2010). In Fig. 6, we over-plot observed temperature differences for station occupations within a few days (L4) or 1–2 weeks (E1) of day 190. Observed differences are generally indistinguishable from the simulated differences.

For a more comprehensive validation, Fig. 7 shows time series of surface–bottom temperature differences observed and (daily) simulated at L4 and E1. The temperature at the depth of the maximum chl *a* concentration is also plotted at E1, confirming the existence of an SCM within the seasonal thermocline. While simulated each year separately, 31 December temperatures of each year are specified as the initial (1 January) temperature of the following year, to ensure continuity across year boundaries. Weak stratification (maximum $\sim 4\,^{\circ}$C) typically is established over ~ 5 months of each summer at L4, while stronger stratification (up to $\sim 7\,^{\circ}$C) develops for longer (by 1–2 months) at E1. Model-observation agreement is remarkably good, with close correspondence between not just surface temperatures, but also bottom temperatures. The seasonally varying stratification at both stations is generally reproduced to within $1\,^{\circ}$C, although high-frequency extremes are under-sampled by weekly (monthly) occupations of L4 (E1), and there is more disagreement at L4. This is most likely because the water column at L4 is strongly influenced by freshwater, with low surface salinity having a substantial effect on stratification.

Vertical salinity structure also explains the apparent temperature instability (negative surface–bottom temperature differences) observed at L4 in winter – the water column is in fact statically stable throughout the time series. The addition of salinity as a model state variable, and first order representation of the coastal freshwater influence, would likely improve the simulation of temperature variability at L4 – we return to this issue in the Discussion.

With some confidence in model performance, in Fig. 8 we show temperature, DIN and chl *a* in sections through the developing tidal mixing front east of Lizard peninsula, along 50.017° N, on days 100, 130, 160 and 190 of 2013. We select this section as representative of CTD transects undertaken annually in late June/early July by University of Southampton fieldwork students. On day 100 (early April), the water column is well mixed almost everywhere, with very weak stratification in temperature evident at 10 km along the section. DIN concentrations are high ($\sim 6\,\text{mmol}\,\text{m}^{-3}$) throughout the water column for bottom depths exceeding a threshold value (~ 40 m), below which PAR falls below a critical value within the water column. As bottom depths become shallower (progressing inshore), DIN concentrations rapidly fall to near zero, where PAR is sufficient at all depths to sustain plankton growth and associated DIN uptake. Inshore chl *a* concentrations are accordingly high (12–13 mg chl a m^{-3}), falling rapidly with distance to background values (~ 0.1 mg chl a m^{-3}) offshore.

By day 130 (early May), the water remains well mixed, although warmer by 1–2 °C, and high productivity has spread offshore, presumably due to intermittent weak stratification during preceding days. By day 160, stratification is clearly established beyond 4 km offshore. DIN concentrations are now reduced to near-zero in the upper 20 m of the stratified water, and high chl *a* concentrations are evidence of the spring bloom. By day 190, stratification has strengthened and DIN concentrations in the deep layer of stratified water columns are further depleted through vertical mixing with the upper photic zone, although surface chl *a* concentrations have by this time substantially declined in the upper layer. The boundary between mixed and stratified waters on days 160 and 190 marks the position of the tidal mixing front. The model has been further used to evaluate the extent of interannual variability around the time of annual fieldwork, in the third week of June. Temperature sections on day 169 of 2002–2013 (see Fig. S7) reveal a wide range of offshore stratification and frontal structure in recent years, with strongest stratification in 2010, weakest stratification in 2011, and a most clearly defined front in 2009.

As an example of the seasonal cycles in temperature, surface DIN and surface chl *a* at four locations across the front (spanning the distance range 3–7 km in Fig. S7), Fig. 9 shows evolution of these variables through 2013. Stratification is very marginal and intermittent at 5.033° W, with surface–bottom temperature differences occasionally reaching 2 °C. DIN concentrations fall close to zero over days 130–300 and chl *a* concentrations are high (in the range 6–8 mg chl a m^{-3} throughout this period. Related to the intermittent stratification are similar fluctuations in chl *a*. This variability is in part attributed to the near-fortnightly spring-neap tidal cycle, which leads to periodic replenishment of nutrients, out of phase with more favourable PAR regimes. Progressing offshore into deeper water, the seasonal cycle transforms towards stronger stratification, a shorter period of surface DIN reduction, and a stronger peak in surface chl *a* around day 150 that corresponds to the spring bloom, followed by substantially lower concentrations during the rest of summer.

3.4 East China and Yellow Seas

Figure 10 shows example fields for a simulation using the East China Sea and Yellow Sea domain with 2013 forcing. Figure 10a shows the annual-mean Hunter–Simpson parameter, $\log_{10}(hu^{-3})$, which falls below 2.7 in particularly shallow regions (see Fig. 1d) that are also characterized by high amplitude tidal currents (see Fig. S2). $\mathrm{Log}_{10}(hu^{-3})$ conversely exceeds 5.0 in the isolated Bohai Sea, lying to the northwest of the Yellow Sea. As for the northwest European shelf, regions with $\log_{10}(hu^{-3}) < 2.7$ remain well mixed throughout summer (Fig. 10b). Elsewhere, stratification is stronger than for the northwest European shelf, with surface–bottom temperature differences on day 190 of $\sim 10\,^{\circ}\mathrm{C}$ across much of the stratified shelf. A major feature of Fig. 10b is the front between mixed and stratified water in the East China Sea that is clearly observed in satellite SST data (Hickox et al., 2000). The simulations also capture the complex system of fronts observed in the Taiwan Strait (Zhu et al., 2013).

The specification of common meteorological variables across $\sim 20^{\circ}$ of latitude and $\sim 15^{\circ}$ of longitude is a considerable approximation, and the annual-mean net surface heat flux field is an important measure of resulting heat imbalances (Fig. 10c). We regard these values as not too excessive, ranging from around $5\,\mathrm{W\,m^{-2}}$ (heat gain) in the far south to around $-10\,\mathrm{W\,m^{-2}}$ (excess heat loss) in the far north (Bohai Sea). Annual-mean carbon production rates in the well-mixed shallow regions of the East China Sea range from 300 to $450\,\mathrm{g\,C\,m^{-2}\,year^{-1}}$, falling to $\sim 100\,\mathrm{g\,C\,m^{-2}\,year^{-1}}$ in the more extensive stratified region (Fig. 10d). These predictions are similar in magnitude to estimates of primary production based on in situ observations (e.g., $145\,\mathrm{g\,C\,m^{-2}\,year^{-1}}$

for “the entire shelf of the East China Sea”, Gong et al., 2003). Monthly-mean surface chl *a* distributions are broadly comparable to satellite observations, although maximum model chl *a* concentrations are generally double those observed, and the spring bloom is ∼ 1 month late, in May rather than April (e.g., for 2013; Figs. S8 and S9). Discrepancies between the model and observations in this region would also be improved by model developments relating to horizontal advection and turbidity close to the coast and to photo-physiology, as described for the northwest European shelf.

To complete the three-dimensional picture, Fig. 11 shows show temperature, DIN and chl *a* concentration in sections through the developing front of the central East China Sea, along 32° N, on days 100, 130, 160 and 190 of 2013. Bottom depth increases considerably with distance offshore. In water of depth < 40 m, the water column remains well-mixed throughout the year, while in deeper water, stratification becomes established between days 100 and 130. In stratified water, DIN is already depleted in the surface layer over days 100–130, and is gradually further depleted in the lower layer over days 130–190 through progressive mixing into the photic zone. A local surface maximum in chl *a* concentration is evident at the frontal boundary (∼ 250 km) on day 130, while a SCM is evident in stratified water on days 160 and 190. The SCM is most clearly defined at ∼ 25 m on day 190.

4 Summary and discussion

We have developed S2P3-R, a versatile framework for efficient modeling of physical and biological structures and processes in shelf seas, adopting an existing 1-D model, S2P3. Here, we compliment ongoing development and use of the 1-D model for specific research hypotheses (e.g., Bauer and Waniek, 2013) and in educational settings, where idealized simulations (e.g., Sharples, 2008) are linked to realistic situations such as fieldwork contexts (e.g., off Cornwall). The S2P3-R framework specifically facilitates research experiments in finely-resolved realistic domains, to test hypotheses regarding the sensitivity of 1-D biogeochemical processes, variously represented, to variations

GMDD
8, 673–713, 2015

of physical forcing on timescales ranging from diurnal to interannual. The framework allows a novel regional and temporal assessment of how vertical physical processes impact primary production and successfully reproduces general patterns in primary productivity and chl *a* in regions where vertical processes dominate, such as tidal mixing fronts and seasonally stratified waters. The S2P3-R framework may also contribute to capacity building in marine monitoring and management for individuals/organisations without the resources to run or analyse complex models of their territorial waters or exclusive economic zones.

We have validated the model in various ways, specifically addressing spatial patterns, vertical structures, and seasonal-interannual variability. 3-D temperature structures are reproduced with considerable success, as are key aspects of the spatial and temporal variability in nutrient and chl *a* concentrations. Differences between the model and observations are informative because, for example, they identify regions in which processes other than those currently resolved in the model are important.

In particular, we note several processes specific to coasts and shelf breaks, of relevance to several aspects of the domains considered here:

- the coastal zone around Cornwall, typified by station L4, is strongly influenced by riverine inputs that promote surface freshening and stratification and alter light attenuation by non-algal particles and dissolved organic matter (Groom et al., 2009; Smyth et al., 2010).

- The northern North Sea is strongly influenced by shelf edge exchange that leads to the inflow of relatively warm and salty Atlantic Water (Huthnance et al., 2009).

- The Yangtze River and two branches of the Kuro Shio – the Taiwan Current and the Tsushima Warm Current – exert strong influences on stratification and productivity in the East China Sea (e.g., Son et al., 2006).

In future versions of S2P3-R, a number of specific enhancements are therefore planned:

GMDD
8, 673–713, 2015
Efficient modelling of shelf seas
R. Marsh et al.

– Implicit divergence of large-scale horizontal heat transport, particularly important near shelf breaks (e.g., northern North Sea).

– Addition of salinity as a state variable, followed by the implicit representation of horizontal salinity gradients associated with coastal runoff.

– Locally enhanced background turbidity associated with coastal runoff and/or shallow water depths.

– Addition of phytoplankton photoacclimation (e.g. Geider et al., 1997).

Further development will formally establish the (presently prototype) option to prescribe spatially-variable initial temperatures and meteorological variables, interpolated appropriately to each model mesh. As an additional diagnostic, the thermal wind balance may be used with the 3-D density field to calculate the residual flows that are associated with tidal mixing fronts (e.g., Hill et al., 2008).

5 Code availability

The S2P3-R (v1.0) framework, comprising source code along with example scripts and output, is available online from: ftp://ftp.noc.soton.ac.uk/pub/rma/s2p3-reg.tar.gz.

Unzipped and uncompressed, the directory/s2p3_reg_v1 contains several subdirectories:

– /main contains the source code, s2p3v7_reg_v1.f90, which is compiled “stand-alone”, and executed using accompanying scripts, with examples of “map” (the Northwest European Shelf simulation, as Fig. 3), “section” (Celtic Sea) and “time series” (E1) simulations (run_map, run_section and run_timeseries, respectively).

– /domain contains bathymetry and tide data for the Northwest European Shelf region (s12_m2_s2_n2_h_map.asc), for a selected north–south section in the Celtic

Sea (s12_m2_s2_n2_h_sec.asc) and for a selected point, E1 in the western English Channel (s12_m2_s2_n2_h_tim.asc).

- /met contains climatological meteorological forcing (Celtic_met.dat).
- /output contains example output data from the three runs (map, section, time series).
- /plotting contains MATLAB scripts for plotting maps, sections and time series (plot_map, plot_section and plot_timeseries, respectively).

The ancillary files needed for simulations in the domains “Around Scotland”, “Western English Channel” and “East China and Yellow Seas”, and for a selection of years, are available on request from the author (e-mail rm12@soton.ac.uk).

The Supplement related to this article is available online at doi:10.5194/gmdd-8-673-2015-supplement.

Acknowledgements. Jeff Blundell assisted with initial editing of the S2P3 source code. Ivan Haigh ran the OSU Tidal Prediction Software to predict tidal current amplitudes in the East China and Yellow Seas. Data at L4 and E1 were downloaded from http://www.westernchannelobservatory.org.uk/data with thanks to the Western Channel Observatory community. R. Marsh acknowledges the support of a 2013 Research Bursary awarded by the Scottish Association for Marine Science. A. E. Hickman was partly funded by a Natural Environment Research Council fellowship (NE/H015930/2).

References

Amante, C. and Eakins, B. W.: ETOPO1 1 Arc-Minute Global Relief Model: Procedures, Data Sources and Analysis, NOAA Technical Memorandum NESDIS NGDC-24, 19 pp., 2009.

Bauer, A. and Waniek, J. J.: Factors affecting the chlorophyll *a* concentration in the central Beibu Gulf, South China Sea, Mar. Ecol.-Prog. Ser., 474, 67–88, doi:10.3354/meps10075, 2013.

Edwards, K. P., Barciela, R., and Butenschön, M.: Validation of the NEMO-ERSEM operational ecosystem model for the North West European Continental Shelf, Ocean Sci., 8, 983–1000, doi:10.5194/os-8-983-2012, 2012.

Egbert, G. D. and Erofeeva, S. Y.: Efficient inverse modeling of barotropic ocean tides, J. Atmos. Ocean. Tech., 19, 183–204, doi:10.1175/1520-0426(2002)019<0183:EIMOBO>2.0.CO;2, 2002.

Egbert, G. D., Bennett, A. F., and Foreman, M. G. G.: TOPEX/POSEIDON tides estimated using a global inverse model, J. Geophys. Res., 99, 24821–24852, doi:10.1029/94JC01894, 1994.

Geider, R. J., MacIntyre, H. L., and Kana, T. M.: A dynamic model of phytoplankton growth and acclimation: responses of the balanced growth rate and chlorophyll *a* : carbon ratio to light, nutrient-limitation and temperature, Mar. Ecol.-Prog. Ser., 148, 187–200, 1997.

Gong, G.-C., Wen, Y.-H., Wang, B.-W., and Liu, G.-J.: Seasonal variation of chlorophyll *a* concentration, primary production and environmental conditions in the subtropical East China Sea, Deep-Sea Res. Pt. II, 50, 1219–1236, 2003.

Hickman, A. E., Holligan, P. M., Moore, C. M., Sharples, J., Krivtsov, V., and Palmer, M. R.: Distribution and chromatic adaptation of phytoplankton within a shelf sea thermocline, Limnol. Oceanogr., 54, 525–536, 2009.

Hickman, A. E., Moore, C. M., Sharples, J., Lucas, M. I., Tilstone, G. H., Krivtsov, V., and Holligan, P. M.: Primary production and nitrate uptake within the seasonal thermocline of a stratified shelf sea, Mar. Ecol.-Prog. Ser., 463, 39–57, doi:10.3354/meps09836, 2012.

Hickox, R., Belkin, I., Cornillon, P., and Shan, Z.: Climatology and seasonal variability of ocean fronts in the East China, Yellow and Bohai Seas from satellite SST data, Geophy. Res. Lett., 27, 2945–2948, 2000.

Hill, A. E., James, I. D., Linden, P. F., Matthews, J. P., Prandle, D., Simpson, J. H., Gmitrowicz, E. M., Smeed, D. A., Lwiza, K. M. M., Durazo, R., Fox, A. D., and Bowers, D. G.: Dynamics of tidal mixing fronts in the North Sea (and discussion), Philos. T. R. Soc. Lon. A, 343, 431–446, 1993.

Hill, A. E., Brown, J., Fernand, L., Holt, J., Horsburgh, K. J., Proctor, R., Raine, R., and Turrell, W. R.: Thermohaline circulation of shallow tidal seas, Geophys. Res. Lett., 35, L11605, doi:10.1029/2008GL033459, 2008.

Holligan, P. M., Williams, P. J. L., Purdie, D., and Harris, R. P.: Photosynthesis, respiration and nitrogen supply of plankton populations in stratified, frontal and tidally mixed shelf waters, Mar. Ecol.-Prog. Ser., 17, 201–213, 1984.
Holt, J., Harle, J., Proctor, R., Michel, S., Ashworth, M., Batstone, C., Allen, I., Holmes, R., Smyth, T., Haines, K., Bretherton, D., and Smith, G.: Modelling the global coastal ocean, Philos. T. R. Soc. Lon. A, 367, 939–951, doi:10.1098/rsta.2008.0210, 2009a.
Holt, J., Wakelin, S., and Huthnance, J.: Down-welling circulation of the northwest European continental shelf: a driving mechanism for the continental shelf carbon pump, Geophys. Res. Lett., 36, L14602, doi:10.1029/2009GL038997, 2009b.
Huthnance, J. M., Holt, J. T., and Wakelin, S. L.: Deep ocean exchange with west-European shelf seas, Ocean Sci., 5, 621–634, doi:10.5194/os-5-621-2009, 2009.
Joint, I. and Groom, S. B.: Estimation of phytoplankton production from space: current status and future potential of satellite remote sensing, J. Exp. Mar. Biol. Ecol., 250, 233–255, 2000.
Kalnay, E., Kanamitsu, M., and Kistler, R.: The NCEP/NCAR 40-year reanalysis project, B. Am. Meteorol. Soc., 77, 437–470, 1996.
Moore, C. M., Suggett, D. J., Hickman, A. E., Kim, Y. N., Tweddle, J. F., Sharples, J., Geider, R. J., and Holligan, P. M.: Phytoplankton photoacclimation and photoadaptation in response to environmental gradients in a shelf sea, Limnol. Oceanogr., 51, 936–949, 2006.
Pemberton, K., Rees, A. P., Miller, P. I., Raine, R., and Joint, I.: The influence of water body characteristics on phytoplankton diversity and production in the Celtic Sea, Cont. Shelf Res., 24, 2011–2028, 2004.
Pingree, R., Holligan, P., and Mardell, G. T.: The effects of vertical stability on phytoplankton distributions in the summer on the northwest European Shelf, Deep-Sea Res., 25, 1011–1028, 1978.
Rees, A. P., Joint, I., and Donald, K. M.: Early spring bloom phytoplankton-nutrient dynamics at the Celtic Sea shelf edge, Deep-Sea Res. Pt. II, 46, 483–510, 1999.
Sharples, J.: Investigating the seasonal vertical structure of phytoplankton in shelf seas, Marine Models Online, 1, 3–38, 1999.
Sharples, J.: Potential impacts of the spring-neap tidal cycle on shelf sea primary production, J. Plankton Res., 30, 183–197, 2008.
Sharples, J., Ross, O. N., Scott, B. E., Greenstreet, S., Fraser, H.: Inter-annual variability in the timing of stratification and the spring bloom in the north-western North Sea, Cont. Shelf Res., 26, 733–751, 2006.

Simpson, J. H. and Bowers, D. G.: Geographical variations in the seasonal heating cycle in northwest European shelf seas, Ann. Geophys., 2, 411–416, 1984, http://www.ann-geophys.net/2/411/1984/.

Simpson, J. H. and Hunter, J. R.: Fronts in the Irish Sea, Nature, 250, 404–406, 1974.

Simpson, J. H. and Sharples, J.: Introduction to the Physical and Biological Oceanography of Shelf Seas, Cambridge University Press, 2012.

Smyth, T. J., Fishwick, J. R., Al-Moosawi, L., Cummings, D. G., Harris, C., Kitidis, V., Rees, A., Martinez-Vicente, V., and Woodward, E. M. S.: A broad spatio-temporal view of the Western English Channel Observatory, J. Plankton Res., 32, 585–601, doi:10.1093/plankt/fbp128, 2010.

Son, S., Yoo, S., and Noh, J.-H.: Spring phytoplankton bloom in the fronts of the East China Sea, Ocean Sci. J., 41, 181–189, doi:10.1007/BF03022423, 2006.

Weston, K., Fernand, L., Mills, D., Delahunty, R., and Brown, J.: Primary production in the deep chlorophyll maximum of the central North Sea, J. Plankton Res., 27, 909–922, 2005.

Zhu, J., Hu, J., and Liu, Z.: On summer stratification and tidal mixing in the Taiwan Strait, Frontiers of Earth Science, 7, 141–150, doi:10.1007/s11707-013-0355-1, 2013.

Table 1. Boundaries, resolution, tidal forcing, initial temperature and meteorological forcing for each domain (POLCOMS = Proudman Oceanographic Laboratory Coastal Ocean Modelling System; OTPS = OSU Tidal Prediction Software).

Domain	Boundaries	Resolution	Tidal forcing	Initial temperature	Meteorological forcing
Northwest European shelf	14.917° W–1.917° E 48.056° N–61.944° N	0.167° (longitude) 0.111° (latitude) (∼ 12 km)	M2, S2, N2 (POLCOMS)	10.1 °C (default)	Daily climatology for the Celtic Sea (Sharples, 2008)
Around Scotland	7.917° W–1.917° E 53.056–61.944° N	0.167° (longitude) 0.111° (latitude) (∼ 12 km)	M2, S2, N2 (POLCOMS)	7.1 °C	Daily NCEP reanalysis data for grid square centred on 0° E, 57.5° N
Western English Channel	4–6° W 49.5–50.5° N	1′ × 1′ (∼ 1 km)	M2, S2, N2 (POLCOMS interpolated)	10.1 °C	Daily NCEP reanalysis data for grid square centred on 5° W, 50° N
East China and Yellow Seas	112–130° E 21–42° N	0.083° × 0.083° (∼ 6 km)	M2, S2, N2, O1, K1 (OTPS)	After 1 year started from 15.1 °C	Daily NCEP reanalysis data for grid square centred on 125° E, 32.5° N

GMDD
8, 673–713, 2015

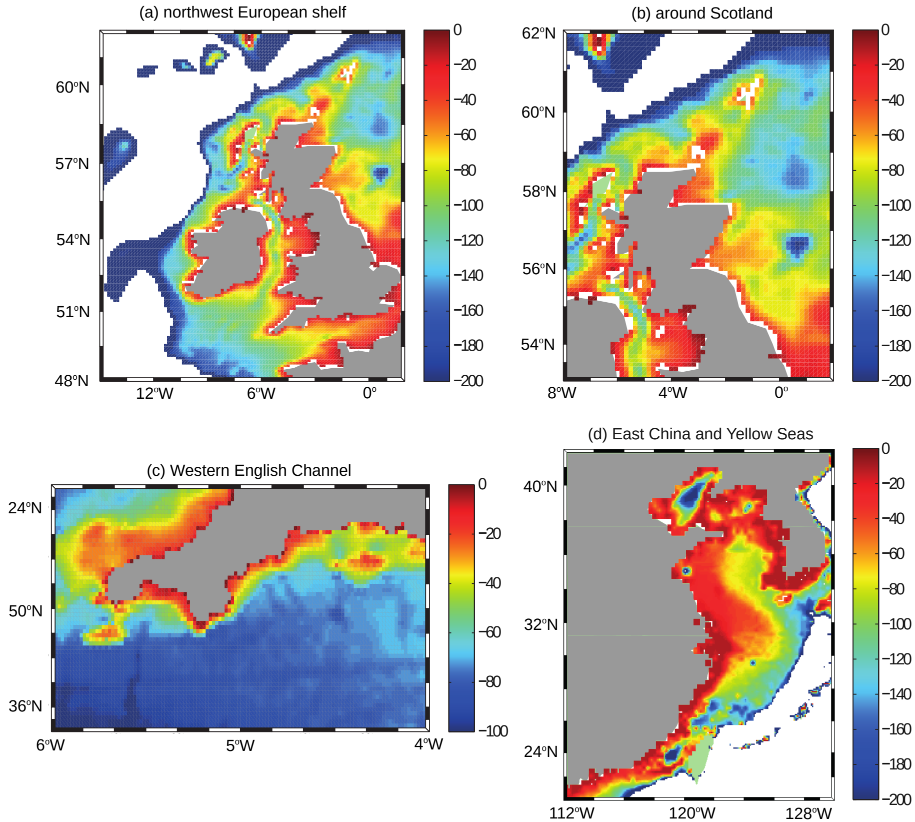

Figure 1. Bottom depth (relative to sea surface) in the four S2P3-R domains: **(a)** northwest European shelf; **(b)** around Scotland; **(c)** western English Channel; **(d)** East China and Yellow Seas.

GMDD
8, 673–713, 2015

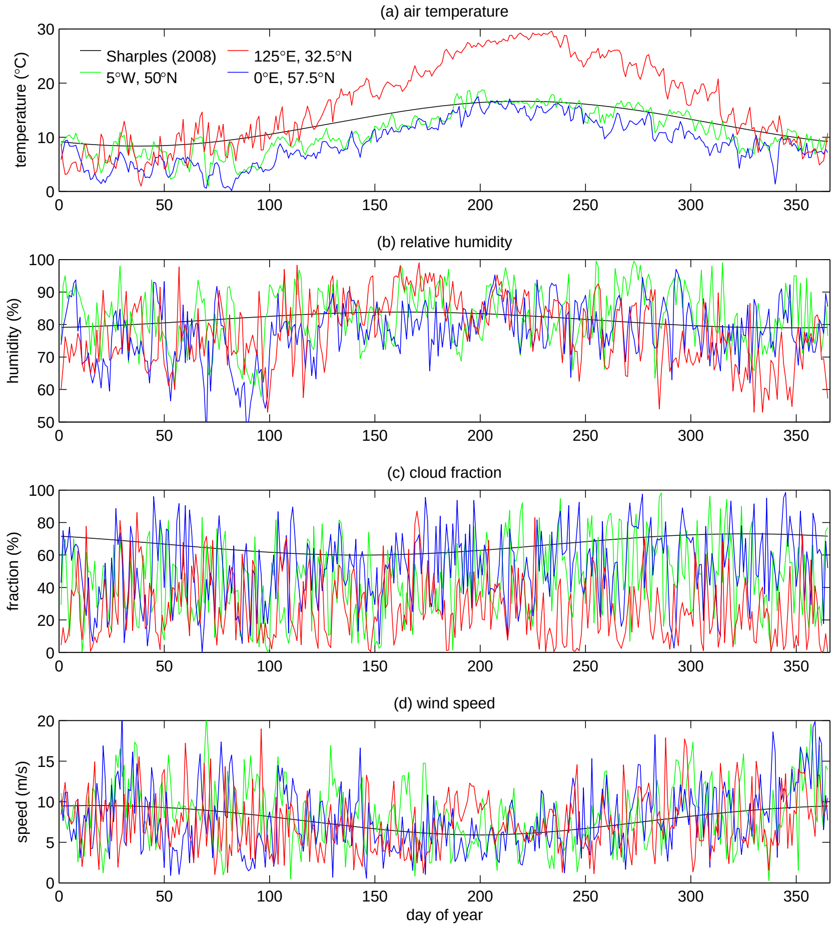

Figure 2. Daily meteorological data: climatological for the northwest European shelf (Sharples 2008), and for 2013 around Scotland, in the Western English Channel and in the East China and Yellow Seas: **(a)** air temperature; **(b)** wind speed; **(c)** cloud fraction; **(d)** relative humidity.

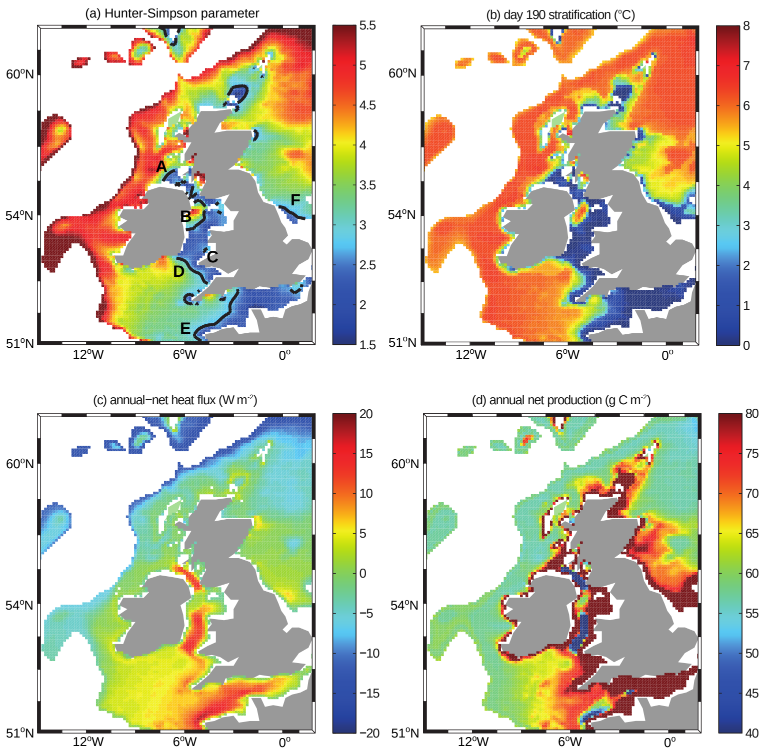

Figure 3. For the Northwest European shelf domain: **(a)** Hunter–Simpson parameter, highlighting the contour delineating $\log_{10}(h\,u^{-3}) = 2.7$; **(b)** day 190 surface–bottom temperature difference; **(c)** net surface heat flux; **(d)** annual net production. In **(a)**, we label fronts as in Fig. 8.1 of Simpson and Sharples (2012): the Islay front (A); the Western Irish Sea front (B); the Cardigan Bay front (C); the St. Georges Channel front (D); the Ushant and Western English Channel front (E). We additionally label the Flamborough frontal system (F).

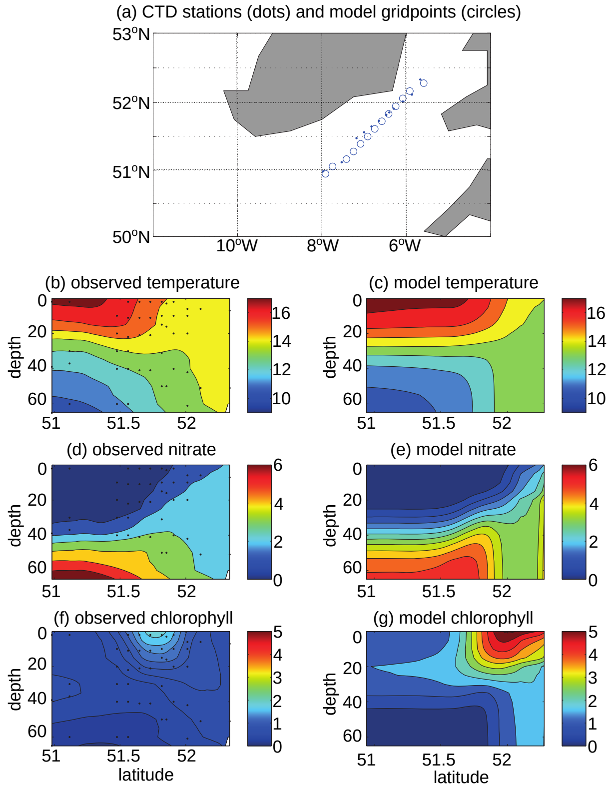

Figure 4. Sections through the Celtic Sea front around day 215 of 2003: **(a)** locations of CTD stations (dots) and model grid-points (circles); **(b, c)** observed and modelled temperature (°C); **(d, e)** observed and modeled dissolved inorganic nitrate (units mmol m^{-3}); **(f, g)** observed and modelled chl *a* concentration (units mg chl *a* m^{-3}). The locations of observations in profile are indicated by dots in (**b**, **d** and **f**).

GMDD
8, 673–713, 2015

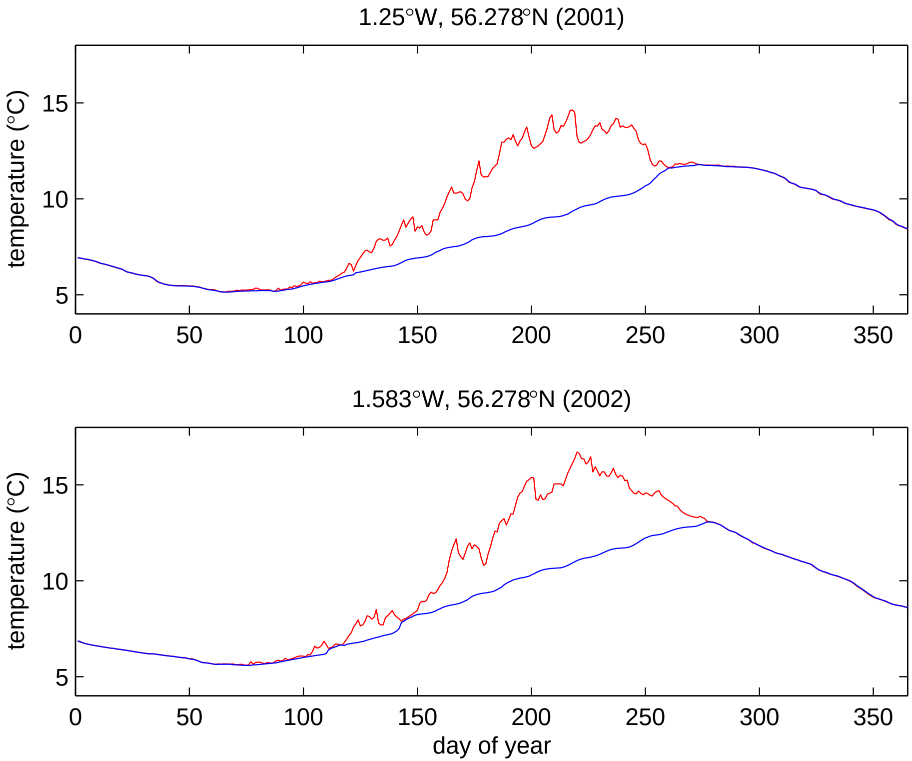

Figure 5. Surface and bottom temperatures (red and blue curves respectively) for the two moorings off northeast Scotland, as simulated in Sharples et al. (2006).

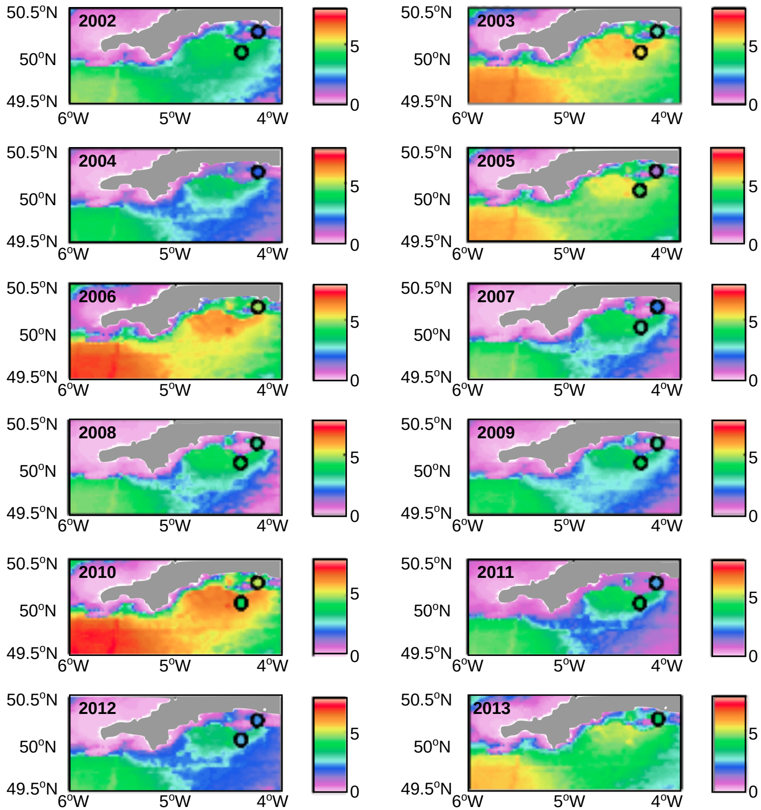

Figure 6. Surface–bottom temperature differences (°C) in the Western English Channel, on day 190 of 2002–2013. Coloured circles indicate the coincident temperature differences at L4 and E1, subject to data availability (E1 data are unavailable in 2004, 2006 and 2013).

GMDD
8, 673–713, 2015
Efficient modelling of shelf seas
R. Marsh et al.

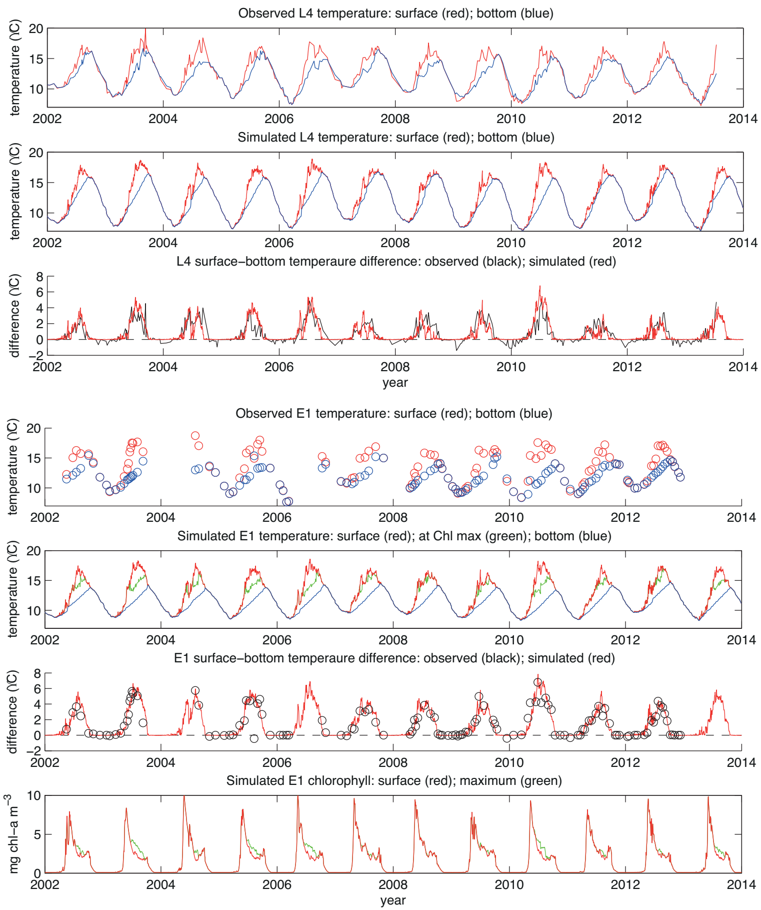

Figure 7. Time series of surface–bottom temperature differences observed and (daily) simulated at L4 and E1 (http://www.westernchannelobservatory.org.uk/data.php).

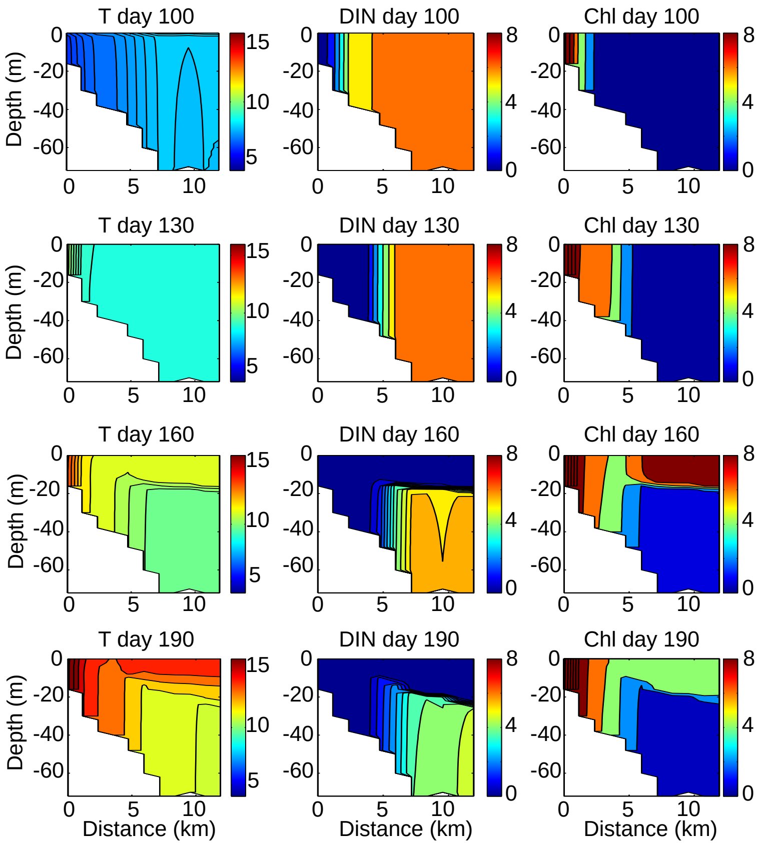

Figure 8. Sections through the developing tidal mixing front east of Lizard peninsula, along 50.017° N, on days 100, 130, 160 and 190 of 2013: temperature (left column); dissolved inorganic nitrate (middle column); chl *a* (right column).

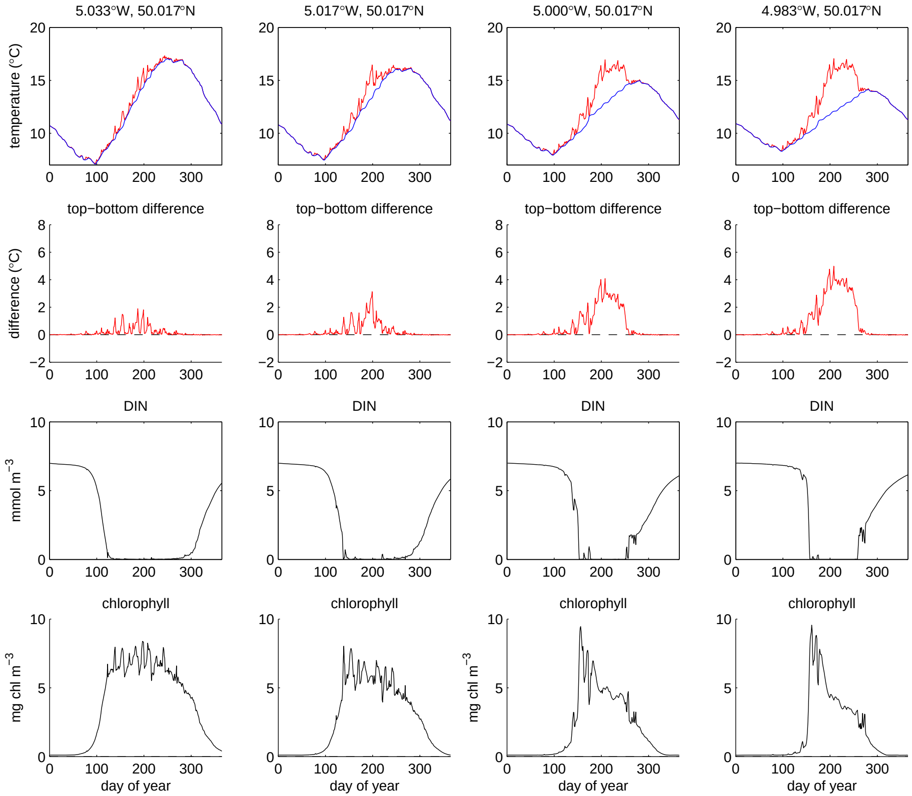

Figure 9. Time series of surface and bottom temperature (red and blue curves), surface–bottom temperature difference, surface DIN and surface chl *a* concentrations, across the tidal mixing front east of the Lizard peninsula in 2013.

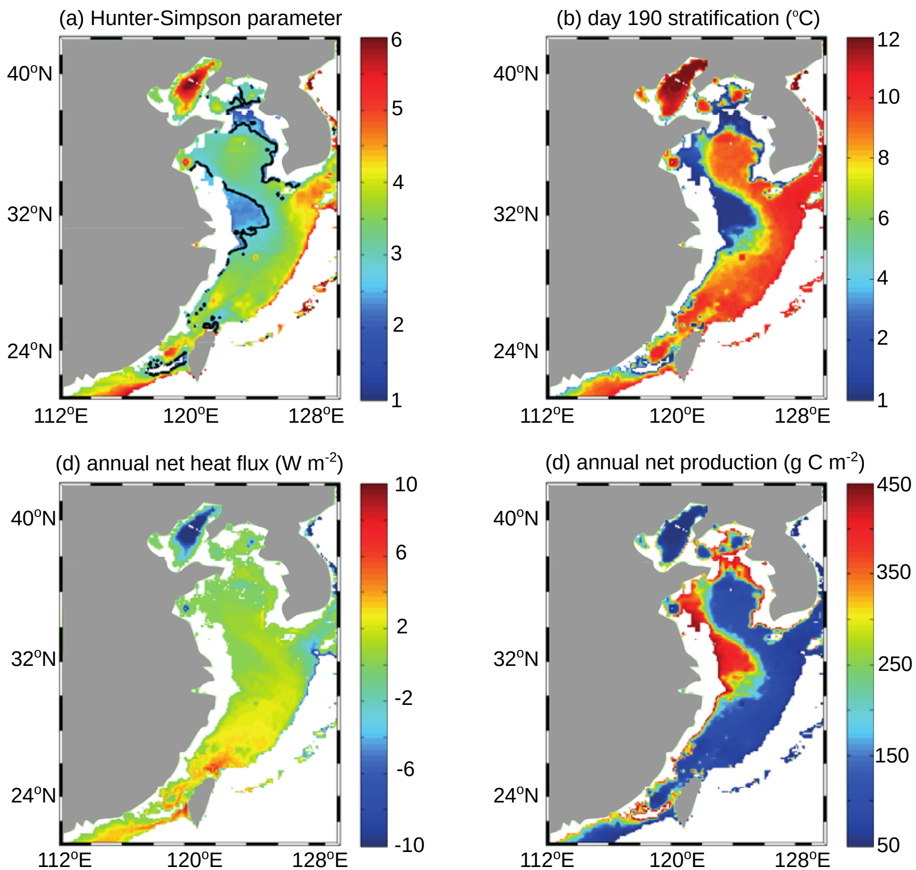

Figure 10. For the East China and Yellow Seas domain in 2013: **(a)** Hunter–Simpson parameter, highlighting the contour delineating $\log_{10}(hu^{-3}) = 2.7$; **(b)** day 190 surface–bottom temperature difference; **(c)** net surface heat flux; **(d)** annual net production.

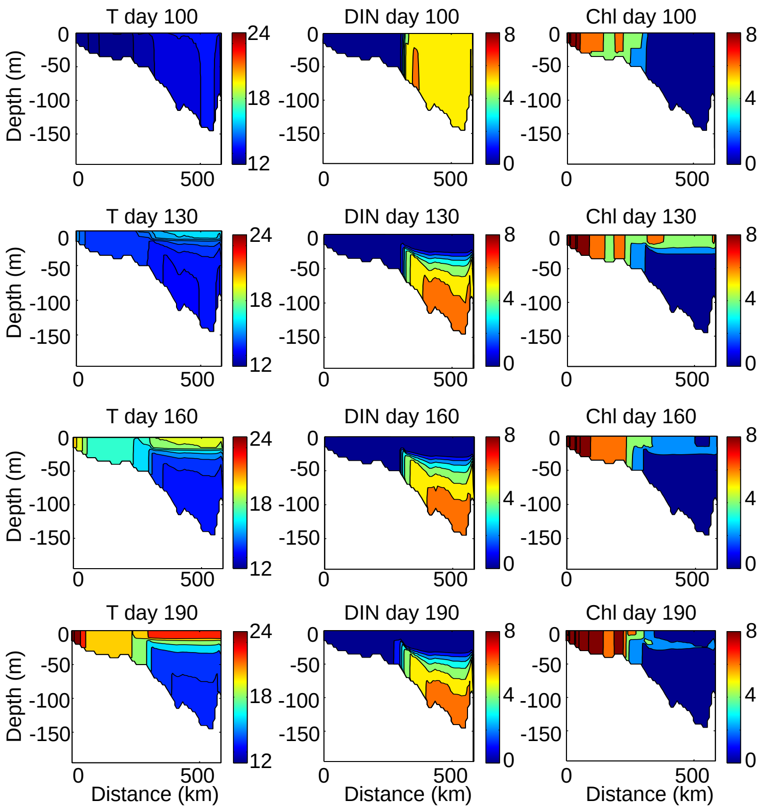

Figure 11. Sections through the developing tidal mixing front of the East China Sea, along 32° N, on days 100, 130, 160 and 190 of 2013: temperature (left column); DIN (middle column); chl *a* (right column).